A new generation of absolute gravimeters

T. M. Niebauer, G. S. Sasagawa, J. E. Faller,
R. Hilt and F. Klopping

Abstract. We describe the design improvements incorporated in a new generation of absolute gravimeters, the FG5. A vertically oriented (in-line) interferometer design is used to remove the influence of floor vibration and tilt on the optical path length. The interferometer uses an iodine-stabilized laser as a primary length standard, with circuitry for automatic peak detection and locking. The seismic isolation system is an active long-period seismometer (Super Spring). The new design has improved passive isolation and thermal drift characteristics over previous systems. Programming flexibility and control of the test mass trajectory have been improved. The computer system has also improved real-time analysis and system capability. The FG5 instrument has a higher level of robustness, reliability and ease of use. These design advances have led to an instrumental uncertainty estimate of $1,1 \times 10^{-8}$ m · s^{-2} (1,0 µGal). Instrument agreement among nine similar devices is 1,8 µGal and observations under optimal conditions exhibit standard deviations of 5 µGal to 8 µGal.

1. Introduction

Surface observations of the gravitational acceleration g provide important geophysical data on the interior density structure of the Earth, localized subsurface lateral density variations, the dynamic compensation of mountain ranges and a host of other geophysical problems. The signal resolution required to resolve spatial gravity variations is of order 20 µGal (1 Gal $\equiv$ 1 cm · s^{-2}). The time rate of change in g for many crustal deformation processes is of order 1 µGal per year or one part in 10^9 per year, and thus an equivalent instrument accuracy is required in order to observe these processes in a few years or less. Gravity measurements provide important control elements in geodetic networks and will play a role in sea-level monitoring. Relative gravity measure-

ments, the basis of a large body of significant work, suf-. fer from problems with calibration, range and drift. Absolute determinations of gravitational acceleration can resolve these instrument issues.

Absolute determinations of g are also essential in a number of metrological measurements. Most notable are calibrations of mechanical force standards such as pressure transducers and load cells. In recent years, researchers have proposed a new mass standard based on electrical references [1]. This device would balance the force of a current (as determined by the quantum Hall effect and the Josephson junction effect) against the weight of a test mass. This application requires knowledge of the absolute value of g at parts in 10^9. Other applications include establishing gravity reference stations for inertial navigation systems.

Absolute measurements of g, at resolutions better than 10^{-6}, were pioneered by the work of Preston-Thomas et al. [2], Faller [3], Sakuma [4], and Cook [5]. Contemporary absolute gravimeters employ laser interferometers that measure the free-fall trajectory of an optical element within an evacuated chamber. Standards for length and time are provided by atomic references, which provide high accuracy and stability. Marson and Faller [6] provide a review of this field.

Three generations of absolute gravimeters have been developed at the Joint Institute for Laboratory

T. M. Niebauer: Micro-g Solutions Inc., 5558 Harlan Street, Arvada, C0 80002, USA.

G. Sasagawa and F. Klopping: National Oceanic and Atmospheric Administration, Geosciences Laboratory, Table Mountain Observatory, 8600 North 39th Street, Longmont, CO 80503, USA.

J. E. Faller: Joint Institute for Laboratory Astrophysics, University of Colorado and National Institute of Standards and Technology, Boulder, CO 80309, USA.

R. Hilt: Department of Physics, Colorado College, 14 E. Cache La Poudre Street, Colorado Springs, CO 80903, USA.
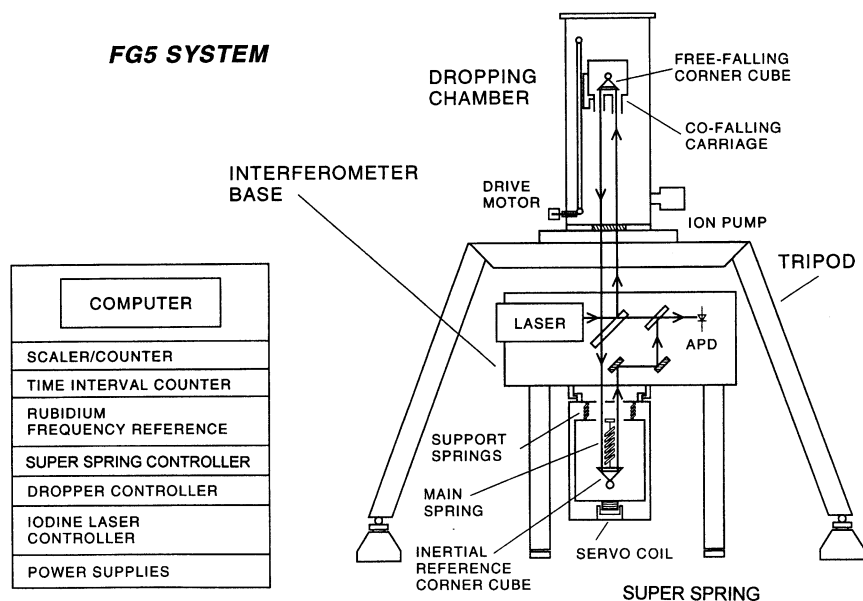
FG5 SYSTEM

DROPPING CHAMBER

FREE-FALLING CORNER CUBE

CO-FALLING CARRIAGE

INTERFEROMETER BASE

DRIVE MOTOR

ION PUMP

TRIPOD

COMPUTER
SCALER/COUNTER
TIME INTERVAL COUNTER
RUBIDIUM FREQUENCY REFERENCE
SUPER SPRING CONTROLLER
DROPPER CONTROLLER
IODINE LASER CONTROLLER
POWER SUPPLIES

LASER

APD

SUPPORT SPRINGS

MAIN SPRING

INERTIAL REFERENCE CORNER CUBE

SERVO COIL

SUPER SPRING

Figure 1. Schematic diagram of key systems in the FG5 absolute gravimeter.

Astrophysics (JILA). The first instrument involved a free-fall test mass and Lamb dip-stabilized laser [7]. The second added a drag-free chamber and an actively isolated inertial reference [8]. The next generation consisted of six gravimeters (the JILAg series) which had improved accuracy and repeatability in the 3 μGal to 5 μGal range [9-11]. The JILAg series instrumental accuracy is at or below the noise level of environmental sources such as barometric pressure variations (of order 5 μGal to 10 μGal) and water table fluctuations (of order 10 mGal or more depending on the set) [12].

The needs of the geophysical and metrological community continue to motivate research and improvements in absolute gravimeters. In 1990, a cooperative effort between academic institutions, government agencies and the private sector was initiated to develop the FG5 instruments. This new instrument design has a target goal of 1 μGal accuracy, along with improved reliability and operation. The first two FG5 instruments were fully operational in February 1993 [13].

2. The FG5 system

2.1 Overview

The FG5 design is based on the previous JILA series instruments, and addresses several known measurement uncertainties at the level of a few parts in 10^9. Technical improvements in operation and reliability have also been implemented in the FG5 design, often motivated by field experience with the JILAg series.

Figure 1 is a schematic view of the FG5 instrument; Figure 2 is a photograph of the same device. The FG5 is
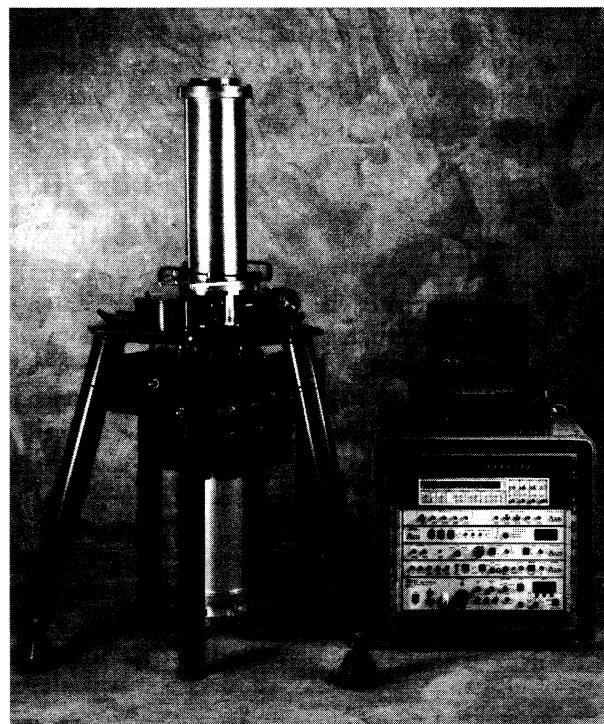
Figure 2. The FG5 absolute gravimeter system in its original configuration. Newer systems have more compact electronics and a smaller computer system, but are essentially identical in measurement performance. The illustrated system utilizes a polarization-stabilized laser.

essentially a modified Mach-Zender interferometer in which one arm of the interferometer traverses a path up to a free-falling corner-cube retroreflector in a vacuum chamber. This beam is reflected back down to a corner cube mounted in the vibration isolated proof mass of an

160

active inertial reference called the Super Spring. The other interferometer arm passes through a beam splitter and recombines with the first beam at a second beam splitter. As the object falls, interference fringes are formed at the optical output. An avalanche photodiode senses and converts the interferometer output to an electrical signal. By counting and timing the occurrences of the fringes, the position of the falling mass is measured as a function of time. Multiple position-time data pairs collected during the drop provide an overconstrained solution to the equation of motion. The FG5 typically collects 200 data pairs over a drop length of 0,20 m (0,2 s duration); a single observation session consists of several thousand drops.

The dropping chamber is a vacuum chamber, maintained by an ion pump at a nominal pressure of 10^{-4} Pa. An optical window at the bottom of the chamber allows the interferometer beam to enter the dropping chamber. The dropped object, an assembly that holds the falling corner cube, resides in a mechanical carriage that serves as a *drag-free* chamber. Before a drop, the carriage is lifted to the top of the vacuum chamber by a small motor. At the start of the drop, the carriage is driven downwards at an acceleration greater than g. The dropped object separates from the carriage and falls freely for $\approx 0,20$ m. Servo electronics sense the displacement between the dropped object and the carriage and maintain a constant separation; the carriage continually tracks the motion of the falling mass, which has no physical contact with the rest of the instrument. At the end of the drop, the carriage gently catches the dropped object and brings it to a stop. The basic concept is described by Zumberge et al. [8].

Besides serving as a method for dropping and gently catching the corner cube, the drag free chamber performs two other important functions. Even at 10^{-4} Pa, residual air molecules exert a small but significant drag on the dropped object. Inside the drag-free chamber, the residual molecules are in free fall along with the dropped object, thus introducing no net momentum transfer. The drag-free chamber is also electrically conductive and shields the dropped object from external electrostatic forces.

Long thin tubes allow the laser beam to enter the drag-free chamber, while restricting the solid angle of residual air molecules infiltrating the chamber. Details of the drag calculations are given in Section 6.1. Although a pellicle window can be used to seal the drag-free chamber, optical wedges in the pellicle introduce systematic errors. The open tubes effectively seal the chamber without using optical components.

The interferometer base is located below the dropping chamber. This subsystem contains the frequency-stabilized laser, spatial filter, collimating optics, and the beam splitters and mirrors required to form the interferometric signal. A fast avalanche photodiode-preamplifier and voltage comparator assembly is housed within the interferometer base. The photodiode has a 50 MHz bandwidth (-3 dB point) and drives a high-speed signal comparator. The comparator generates digital pulses which are counted and timed in an external electronics rack.

To reduce the data variance the reference corner cube must be isolated from ground vibrations. The reference corner cube is integrated into the seismometer proof-mass of the Super Spring, which is mounted directly below the interferometer base. Servo electronics generate a force feedback that tends to remove ground motion in the first stage before it is transmitted to the proof mass on the second stage. Effective free periods in excess of 60 s can be obtained. The Super Spring employs a new passive method that compensates for thermal drifts in the spring length. Details of the Super Spring design have been described by Rinker [14] and Nelson [15].

A separate set of transport containers house control and support electronics. These subsystems include a rubidium atomic frequency standard, stabilized-laser controller, servo electronics for the drag-free chamber and Super Spring, data acquisition electronics and a notebook microcomputer. An 80×86 based PC computer controls data acquisition and performs real-time processing of the gravity data. Power supplies and distribution buses are also located in the electronics system.

The current FG5 system consists of one electronics rack, three cases of mechanical components, and a small carrying case for the notebook computer, docking station and printer. In its current configuration, the FG5 absolute gravimeter requires less than 500 W of electrical power. A single operator can assemble the gravimeter and acquire data in about an hour.

Many basic instrument systems in the FG5 are unchanged from those in previous absolute gravimeters. However the practical lessons of the past have been applied to the FG5 system. The electronics hardware (connectors, panel switches, cables, etc.) are more robust. Improved locking mechanisms have been designed into the moving components of the system. Shipping containers are well padded to deal with mechanical vibrations and shocks encountered in transit.

The accuracy improvements have been achieved through a number of unique and significant design changes, which are discussed below.

2.2 In-line interferometer system

The largest systematic optical error in the JILAg series and other absolute gravimeters is systematic tilt coupling. The test interferometer arm of the JILAg Michelson interferometer terminates at the free-falling test mass and the reference arm ends at the inertial reference object; the two arms are horizontally displaced by 0,2 m. Any tilting of the interferometer couples into the

vertical path length and thus introduces an optical path length perturbation. The release of the test mass causes the instrument to recoil, thus tilting the floor and the gravimeter interferometer. In the JILAg system a 1 nrad tilt occurring during the drop generates an error of order 1 µGal. The measurement is not as sensitive to constant angular offsets from the vertical plane, which cause alignment errors with a cosine dependence. A constant angular displacement of 45 µrad introduces a 1 µGal error. The most troublesome tilts are those that occur during the drop and are coherent in phase at frequencies from 1 Hz to 100 Hz. Typical separations of the tripod feet are of order 1 m, so tilts of order 1 nrad introduce vertical displacements of order 1 nm, which can in turn introduce systematic *g* errors. Tilt coupling errors are almost as large as direct vertical displacement coupling in such systems and are highly site-dependent. In the JILA gravimeters, it is not uncommon to observe biases of 5 µGal to 30 µGal due to the tilt coupling.

It is clear that a good interferometer design should eliminate or minimize coupling to horizontal, vertical and tilting motions of the fixed optical elements (including the laser). This can be done by keeping the test and reference interferometer arms in a vertical line. This obeys the Abbe rule that optical measurement systems should be in line with the measurement axis. There are many possible in-line interferometers but we have chosen a modified Mach-Zender for the FG5; this has good optical design characteristics and satisfies practical considerations of size, weight and rigidity. The residual tilt noise that is observed in the JILA systems is greatly reduced in the FG5 instrument.

The FG5 system is a potential vertical "in-line" interferometer, as illustrated in Figure 3, which is insen-

sitive to tilts and other motions of the interferometer base during the drop. The reference beam of the interferometer travels through the primary beam splitter, while the test beam is reflected up to the test mass corner cube. The test beam is then reflected back down through the primary beam splitter. The beam splitter has a reflective coating over only half of the front surface, maximizing transmission of the test beam. The test beam then passes into the retroreflector in the Super Spring inertial mass. The return beam is reflected by pickoff mirrors, and is recombined at the secondary beamsplitter with the reference beam, forming the interferometric signal. This interferometer design is insensitive to translations and rotations of the optical block containing the two beam splitters and pick-off mirrors.

Our in-line interferometer provides three interferometric outputs after the second beam splitter; the outputs are schematically represented in Figure 4. One output is used to detect fringes with the photodetector assembly. The other interferometric output undergoes multiple reflections and refractions in the optical flat, the *attenuator*, at such an angle that the beam undergoes four internal reflections. The directly transmitted beam illuminates a frosted glass plate with the fringe pattern; this is used for interferometer alignment. The second transmitted beam is unused.

The third, and final, transmitted beam is used to align the test beam with the local vertical gravity vector. A pool of a fluid such as alcohol is placed on top of the Super Spring; this serves as a horizontal mirror which reflects the downwards travelling beam back up to the first beam splitter. The beam then travels directly through the second beam splitter and then through the attenuator and recombines with the directly transmitted reference
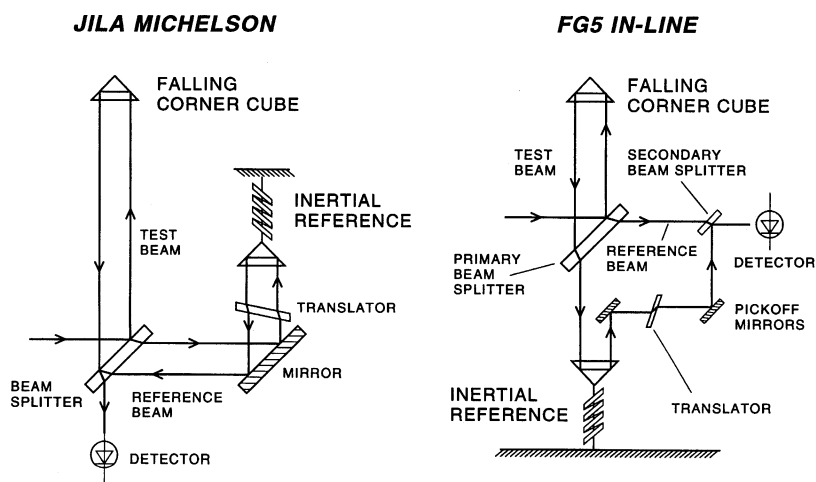
JILA MICHELSON　　　　　　　　　　**FG5 IN-LINE**

Figure 3. Conceptual drawing of the in-line interferometer system. The JILA series Michelson interferometer is also shown for comparison.
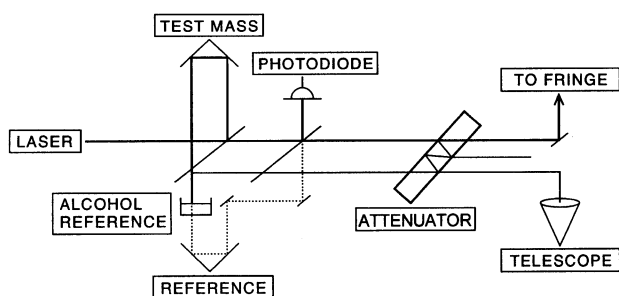
Figure 4. Schematic diagram of the various optical outputs and subsystems of the FG5 interferometer assembly.

beam. The angle of incidence and thickness of the attenuator optical flat were chosen to overlap the two beams; the optical coatings were chosen to match the intensity of the test and reference beams. These two beams are observed with a Wild-Leitz T2 telescope in order to measure the collimation. The test beam and reference beam are collimated only when the test beam is vertical. The test beam verticality must be set to within 44 μrad to avoid a measurement error of 1 μGal. The collimation output port is also useful for setting the angular alignment of the test and reference beams for maximum fringe contrast.

The in-line interferometer mounts critical optical elements in a small, highly rigid kinematic block. The high mechanical rigidity of the interferometer block ensures that the fixed arm length does not move appreciably during the time of a drop. Stable, high resolution optical mounts make it possible to steer the pickoff mirrors and the translation window, and so provide a sufficient number of degrees of freedom to generate a proper interferometric pattern.

Optical materials and mountings have been improved dramatically, increasing stability and easing alignment procedures. The FG5 series uses corner cubes with wavefront distortion limited to $\lambda/6$. For comparison, the JILA instruments employ $\lambda/4$ surface corner cubes. Mirror and beam splitter specifications are typically $\lambda/20$. The mechanical design of the optical mounts has been improved over those used in the JILAg systems. The main body of the interferometer base is a single aluminium casting, with machined surfaces for optical mounting and surface finish. The casting has better stress relief and correspondingly weaker resonances than would a similar machined piece, and is also lighter and easier to manufacture.

2.3 Laser system requirements

The goal of 1 μGal accuracy requires a length standard with a minimum accuracy of 1 part in 10^9. This standard is realized using frequency-stabilized lasers, typically exhibiting accuracies ranging from 2 to 3 parts in 10^9 to a

few parts in 10^{11}, depending on the particular stabilization scheme used. The best stabilized lasers are based on atomic hyperfine transition absorption features and, until recently, were fragile laboratory devices. The JILA instruments use polarization-stabilized lasers that suffer from ageing and temperature effects [16], dual frequency leakage [17], and the need for frequent calibrations with respect to known standards. The FG5 uses two new laser designs, both of which are improvements over the original JILA design.

2.3.1 Polarization-stabilized AL-1 laser

The AL-1 polarization lasers are similar in principle to the original JILA series lasers. This laser is frequency-stabilized by matching the intensities of two linear, orthogonally-polarized modes lasing simultaneously with a frequency separation of order 720 MHz. The laser's stability relies on the stability of the centre frequency of the gain curve. Under laboratory conditions a drift of 5 MHz/year can be realized. The frequencies of the two modes, and thus the gain curve centre frequency, are regularly calibrated against iodine laser standards. Errors in calibration and laser variations introduce errors of 2,07·μGal for each 1 MHz of error in the optical frequency.

Ideally only one of the two frequencies exits the laser. However, imperfections in the optics mix these frequencies in the output beam. These two frequencies give rise to separate interference contributions that systematically perturb the interferometric phase measurements by several parts in 10^8 for a 99 % mode purity. Perturbing influences such as magnetic fields can degrade the orthogonal polarization of the modes, leading to a deterioration of the mode purity. This is avoided in the FG5 by mounting the laser far from magnets in the Super Spring and ion pump. A new version of the laser with a mode purity of better than 99,9 % was developed for the FG5 gravimeter.

Although the stability of the polarization-stabilized laser does not strictly meet the requirement for 1 μGal accuracy, periodic calibrations of the laser against a more stable reference allow effective use on the FG5. The inconvenience of calibration is somewhat offset by the relative ruggedness, reliability and low cost of the laser.

2.3.2 Iodine-stabilized primary reference laser

The FG5 system can also use a rugged version of an iodine-stabilized laser, WEO Model 100, that locks an optical frequency to hyperfine transitions in $^{127}I_2$ [18]. The hyperfine transition levels are highly stable with respect to external influences. The iodine laser is a practical realization of the SI definition of the metre and thus requires no calibration. It is the one of the most common

absolute optical frequency standards in use today, with an absolute accuracy of 2,5 parts in 10^{11} or an equivalent accuracy of 0,2 μGal [19]. The WEO Model 100 is fundamentally a laser gain tube and iodine absorption cell within an optical resonant cavity. The cavity is modulated and third harmonic detection is used to lock the cavity length on a selected absorption peak.

The WEO Model 100 system prototype was developed at the Bureau International des Poids et Mesures (BIPM) and it has several unique features [18]. The laser cavity mirrors are mounted in an Invar cylinder for stiffness and thermal stability, and Peltier elements are used to stabilize the Invar cylinder against changes in temperature. The mirror mounts are robust and the laser can be handled rather roughly without requiring realignment.

Automatic circuitry selects and locks the laser on a specific iodine peak. The dc level of the absorption curve, normalized for laser intensity, is used to measure and identify the specific range of an absorption peak. Once an appropriate range is found, the second and third absorption peak derivatives are used to lock the laser. Without the auto-locking circuitry, the laser would require constant manual monitoring and re-locking.

2.3.3 Effect of laser modulation

The WEO Model 100 laser output is single mode so there are no two-frequency problems as with polarization-stabilized lasers. However, the modulated output introduces problems for interferometers with unequal path lengths. The FG5 in-line interferometer design has a large path-length difference between the test and reference beams, of order 2 m.

Iodine-stabilized lasers dither the optical frequency over a range of 6 MHz at a rate of 1,2 kHz. The path length imbalance introduces a large delay time in the test beam, and the interferometer output thus has a dithered frequency output. The phase shift between the reference and test beam x_1 has a time-dependent part proportional to the changing path difference. The phase shift written in terms of the path difference is

$$\Delta\phi = \frac{f_0\Delta x\lambda}{c}\sin(\Omega t),$$

where f_0 is the modulation amplitude (≈ 3 MHz), λ is the nominal wavelength, and Ω is the modulation frequency, which is ≈ 1170 Hz. A temperature-compensated crystal oscillator serves as frequency standard and is stable at 10 parts in 10^6. The path difference $\Delta x = \Delta x_0 - gt^2/2$ has a constant term Δx_0 of 2 m due to the initial path difference and a time-dependent component due to the falling corner cube. The interferometric output exhibits a sinusoidal signal at the modulation frequency with a small amplitude decrease over time. In Figure 5a the effect of the modulation is observable as 10 nm residuals
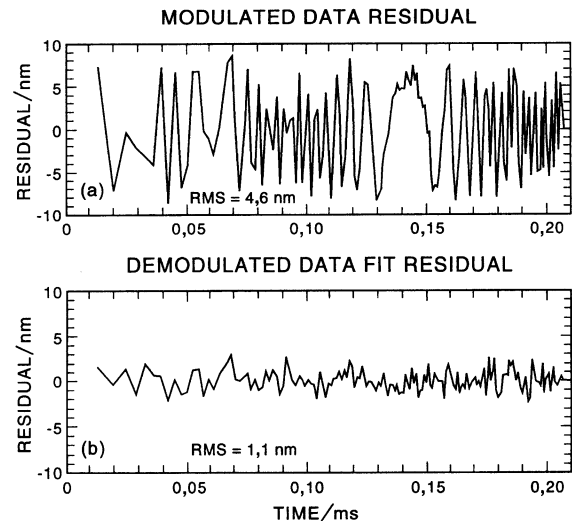

Figure 5. (a) Data residuals for a fit that does not correct for the frequency dither in the iodine-stabilized laser. (b) Data residuals after the dither has been removed in the least-squares fit.

in the fitted signal. Beats are observed when the sampling frequency matches a multiple of the modulation frequency. Figure 5b shows the residuals of the same signal after fitting an additional sinusoidal function with the known dither frequency. The least-squares fitting algorithm fits simultaneously for the dither amplitude and phase. Numerical simulations show that the parameter estimates from this method are unbiased, and are insensitive to errors in the dither frequency at the level of some parts in 10^3.

2.3.4 Laser isolation

Optical feedback can send the WEO Model 100 servo system out of lock. Initial designs of the FG5 system used a combination of a quarter-wave plate and a linear polarizer for feedback attenuation. This method worked well with AL-1 lasers but was insufficient for the WEO Model 100 lasers. A Faraday isolator works far better for the iodine-stabilized lasers. We have confirmed that the magnetic field from this device does not affect the measured value for g.

3. Dropping chamber and controller

The dropping chamber is based directly on the JILA series gravimeters. Mechanical design changes concerned primarily with its construction and assembly led to a reduced gas load and correspondingly improved vacuum level. The vacuum conductance of the ion pump mounting and valve assemblies has been dramatically increased. The travel lock assembly was also improved, improving the robustness of the system.

164

The system controller is a hybrid digital-analogue control system. Analogue servos track the appropriate signals during the measurement phase, while a digital system selects the appropriate analogue servo loop to close. A state machine implemented in an EPROM buffer controls the mechanism, and can be programmed for a variety of control modes.

The FG5 design includes the option to throw the mass, and thus conduct a symmetric rise and fall measurement. Such a measurement has the advantage that frequency-dependent phase delays in the timing electronics tend to cancel (although not perfectly) on the rise and fall portions of the drop. The measurement also samples over a longer time and distance interval, without using any additional space. However, tests show that the initial launch conditions are difficult to control, and as a result the translation and rotation of the dropped object are generally unacceptable. Moreover, the instrument setup is far more demanding in order to throw the mass. The drag-free chamber path must be aligned with the vertical to within 0,1 mrad in order to minimize the horizontal velocity and keep subsequent Coriolis accelerations below 1 µGal. The symmetric rise and fall measurement remains an interesting goal.

4. Inertial reference mass

The Super Spring system provides a vibration isolated platform, buffering the reference corner cube and the measurement from seismic noise [14]. The Super Spring concept has proved highly effective in reducing the data variance of the JILA series gravimeter.

The primary support stage of the FG5 Super Spring employs flexures in an equilateral triangle arrangement found in some commercial seismometers. The support flexure arrangement is quite rugged and does not have the nonlinear behaviour about the equilibrium point of the original Super Spring's flat flexure design.

The new Super Spring is 46 cm high, half the size of the original prototype, with similar passive isolation and better active isolation. This was accomplished through improvements in the flexure design, spring materials and electronics.

The JILAg Super Spring is 90 cm long, in order to accommodate the main spring assembly. Its main spring is fabricated from Ni-Span C, an alloy with a low thermal expansion coefficient. However, Ni-Span C has a relatively low yield strength. Thus, in comparison to a steel spring, a Ni-Span C spring reaches its elastic limit when supporting a smaller mass. Thus the spring must employ more coils to achieve the same free period. The free length of a Ni-Span C spring is relatively long, about 23 cm to support a 300 gm mass with a 1 s period. In addition, Ni-Span C must be heat treated during fabrication, which removes any spring pre-tension. With other materials, the spring extension can be decreased by

winding the spring with pre-tension, producing a "negative" unloaded length.

The new FG5 Super Spring uses piano wire (tempered steel), that has a much greater shear modulus and allows for a shorter spring with considerable pre-tension. The thermal expansion of the spring is compensated by a simple fluid expansion reservoir (aneroid bulb). As the temperature increases, the main spring sags and the fluid expands. This expanding fluid pushes up against the top flexure support assembly and thus raises the spring. The bellows is positioned on a mechanical lever so that the thermal properties may be matched to give a very small effective thermal coefficient of expansion (we have succeeded in obtaining a temperature coefficient of $3 \times 10^{-5}/°C$, equivalent to aluminium). The top flexure support assembly is also a convenient location for the coarse adjustment motor.

The Super Spring controller is also improved through the elimination of dc feedback. Previous versions of the Super Spring had dc feedback-induced drift problems, which necessitated occasional manual adjustment of the spring support point. The new system requires less frequent adjustments.

5. Signal detection and data processing

Timing precision has also been improved in the system. The fringe signal is detected using a high-speed avalanche photodiode (RCA CD30950E), with a responsivity of $\approx 3 \times 10^5$ V/W at 630 nm and a bandwidth of 50 MHz (-3 dB point). The same circuit board employs an ac-coupled high-speed comparator (AD 9696) to generate digital pulses at fringe signal zero crossings. The TTL compatible signal is then transmitted down a coaxial line to matched 50 Ω terminated inputs on the time interval counter. Previous absolute gravimeters sent the analogue fringe signal through a coaxial cable to a comparator in the electronics rack. It was essential to keep this cable short so that phase shifts did not bias the gravity value. In the FG5, the comparator is placed on the photodetector board and a digital signal is transmitted through the cable to the timing electronics. At first glance the benefits of this method are unclear, as any stray capacitive coupling distorts digital pulse edges more than analogue sine wave signals. However, the phase shifts of the digital edges remain constant as the fringe signal sweeps from dc to 6 MHz in 0,2 s. We have shown that 30 m cables do not shift the gravity values observed with the FG5 whereas 6 m cables introduce 10 µGal errors in the JILAg systems.

The analogue photodiode signal is capacitively coupled to the comparator through a single-pole high-pass RC filter. The question of measurement error due to frequency-dependent phase shifts is discussed in the section on error analysis.

The time interval counter used is the Stanford

SRS620. This counter has an improved least count resolution over the counters used with JILA series instruments (from 256 ps to 100 ps). The internal clock is phase-locked to a rubidium frequency reference. The dynamic range of the scalar/counter, which prescales and stores the fringes observed, is greater than that of the JILA systems.

The data acquisition system employs 80×86 PC computers, typically 80386/80387 or 80486 based systems. This choice of computer provides more than adequate computing resources for field operations. The PC architecture is also easy to upgrade with additional hardware such as mass storage devices (i.e. tape streamers or magneto-optical floppies) and A/D cards.

Control and processing software is much more sophisticated and comprehensive than in other gravimeters. The data are least-squares fit to a function that uses a known a priori vertical gravity gradient in the fourth-order equation of motion [20].

$$x_i = x_0 + v_0 + \tfrac{1}{2} g_0 \tilde{t}_i^2 + \tfrac{1}{6} \gamma v_0 \tilde{t}_i^3 + \tfrac{1}{24} \gamma g_0 \tilde{t}_i^4$$

$$\tilde{t} = t_i - \frac{(x_i - x_0)}{c},$$

where x_0, v_0 and g_0 are the initial position, velocity and acceleration at $t = 0$, γ is the vertical gravity gradient and c is the speed of light. This fit is linear in the trajectory parameters and accounts for both the time delay due to the finite speed of light and the effect of the local gravity gradient. Nonlinear methods to extract the gravity gradient and trajectory parameters simultaneously have proved difficult to implement as signal-to-noise levels are low. Appendix 1 discusses the equation of motion in greater detail.

Errors in determining the vertical gravity gradient can be approximated by use of effective height of measurement rules. If a second-order polynomial is used as the equation of motion for the trajectory data, then the acceleration estimate obtained is equal to the instantaneous acceleration at a point approximately $5/16 L$ down from the starting point, where L is the total length of the drop. If the drop length is 0,2 m and the vertical gravity gradient equals the free air gradient (3,086 μGal/cm), then a 1 % gradient estimate error introduces a 0,19 μGal error in the absolute gravity estimate. Note that gradient estimates are derived from relative gravimeter observations and are thus not included as intrinsic error contributions in absolute measurements.

The finite speed of light gives a correction for the calculated gravity signal since the optical interference occurs at time $\Delta t(t) = L(t)/c$ after the light bounces off the dropped object. For the simplest case with no gradient the functional form is a parabola with a retarded time $g(t + \Delta t)^2/2$. The bias is given approximately by $g^2 t^3/2c$, and introduces an apparent shift of -11 μGal (1 part in 10^8) in the gravity value of a 20 cm drop. The speed of

light correction has actually been measured in a differential free-fall measurement (a gradiometer) where both objects were allowed to free fall with different initial velocities [21]. In gravimeters this effect cannot be directly observed but it can and should be removed by fitting the data using the retarded times.

Any relativistic effects (other than the retarded times corrections) are minuscule. Effects at a level of 10^{-10}, such as length contractions or simultaneity, would require relative velocities in excess of 1000 m/s to become a problem.

The numerical approach to solving this over-constrained least-squares problem employs a Householder or QR reduction, that provides a solution in an efficient and numerically stable manner. In particular, this method does not require accelerating local reference frames, scaling, or centring of the times around the mean to produce numerically accurate results.

In-field computations account for the solid Earth tides, polar motion, barometric pressure, ocean loading and transfer from the observation height to a preferred datum height. Statistical estimates computed include the mean, median, covariance error estimates and standard deviations of the data sets. Graphics display the residuals of the least-squares fit, the gravity time series and distribution histograms, as well as various operating parameters and environmental sensor readings. The system can also monitor the rotation and translation of the test-mass in real-time as a diagnostic or veto data as unsatisfactory. All the digital data from the instruments, including all fringe x-t pairs, are recorded on disk in a binary format. Except for the tidal corrections, the data processing conforms to IAGBN standards.

The recommended Tamura tide program, when integrated with the field program, exceeds the memory management capabilities of the existing code compiler. The tide program used agrees with the Tamura program to better than 2 μGal. Thus, the maximum disagreement for any one point observation is 2 μGal; errors due to the tidal program average towards zero when observations are integrated over more than 24 hours. At the time of publication, a new compiler release is expected to resolve this problem.

6. Instrumental uncertainty estimates

The uncertainty budget analysis attempts to determine the instrumental uncertainty contribution through calculations and measurements of known physical effects that degrade the instrument accuracy. The budget is based on the reasonable assumptions that the instrument is in good working condition and is properly operated. In the following calculations, terms are typically carried out to four significant figures. The subsequent uncertainty estimates are rounded up to the nearest 0,1 μGal. Much of the basis of this work may be found in the theses of

Faller [3], Hammond [7], Niebauer [22] and Zumberge [23].

The measurement uncertainty budget is difficult, if not impossible, to prove rigorously. One problem is that though all the instrument uncertainty terms are small, of order 10^{-9}, many are difficult to estimate or measure reliably. In some cases, the gravimeter is more sensitive than other existing instruments that could be used to quantify these effects. Finally, one can never be absolutely sure that some unrecognized effect is not present. For these reasons, the FG5 uncertainty estimate is subject to future revision.

6.1 Vacuum requirements

The vacuum pressure in the dropping chamber is typically lower than 1×10^{-4} Pa. At this pressure the mean free path of an air molecule is greater than the diameter of the vacuum chamber and the drop length. It is therefore appropriate to use simple statistical mechanics calculations. Here we estimate two different effects of residual gas molecules: drag forces and outgassing from the dropped object.

6.1.1 Drag effect

The drag force F_d on the falling mass, at low pressures, is calculated [24] as

$$F_d = A\rho v V/4,$$

where ρ is the gas density, A is the total surface area of the mass, v is the object's velocity and V is the mean gas particle speed. The maximum velocity of the object during a 0,2 s drop is ≈ 2 m/s. The test mass is a cylinder with a 34 mm diameter, length L of 9,375 cm (total surface area of 118,3 cm^2) and a mass of 100 gm. The mean gas velocity V for molecules of N$_2$ is about 476 m $\cdot$ s^{-1} at a temperature $T = 300$ K. The mean gas density is evaluated with the ideal gas law:

$$\rho = \frac{mP}{kT} = 1,497 \times 10^{-9}\, kg \cdot m^{-3},$$

assuming a nominal pressure of $1,33 \times 10^{-4}$ Pa (1 μ torr); m_r is the relative molecular mass of diatomic nitrogen.

Evaluating the fractional error in acceleration, a, due to residual gas drag forces yields a value of $a/g = 4,22 \times 10^{-9}$ or a 4 μGal error without a drag-free chamber.

The co-falling drag-free chamber (cart) provides a molecular shield for the dropped object. Residual molecules inside the cart move with the same average velocity as the cart walls and do not result in drag forces on the dropped object. The cart is not totally sealed, however, because it has two *collimating* tubes on the bottom, and one on the top, to permit laser beams to penetrate the cart

and reflect off the dropped object within. The tubes on the top and bottom also help to minimize the differential vacuum conductance. The collimating tubes present a total cross-sectional area of 1 cm^2, with a length of 4 cm. The effective forward cross-section of the dropped object is thus reduced by a factor of about 0,002, yielding a net drag induced acceleration of 0,01 μGal.

6.1.2 Outgassing of the dropped object

Now consider the outgassing effect on the dropped object. The FG5 system typically operates at $1,3 \times 10^{-4}$ Pa with a full rated pumping speed of 8 l/s at the ion pump inlet. The ion pump conductance into the dropping chamber is high as there are no baffles, so the actual pump speed is close to the full rated pump speed. The total mass flux Q is estimated to be $1,333 \times 10^{-11}$ kg/s.

The dropped object has a total surface area of 118,3 cm^2 and the vacuum hull is a cylinder 15,2 cm in diameter by 62,2 cm high. The surface area ratio R_{sa} is thus (118,34 cm^2)/(3392 cm^2) or 0,0354. The mean molecular speed is 476 m/s. Thus the acceleration experienced by the mass, M, due to its proportional share of the outgassing rate is

$$a = \frac{Q_c V}{M} R_{sa}$$

or 0,225 μGal. This is a pessimistic estimate. Leaks must be responsible for a significant fraction of the equilibrium pressure, and plastic components in the vacuum system (which are not part of the test mass) are the largest contributors to the outgassing. Furthermore, the outgassing molecules from the dropped mass do not travel in the same direction, reducing the net momentum transfer. A conservative evaluation of the outgassing effect scales the above figure by a factor of 1/3, yielding a possible error estimate as 0,075 μGal.

The sum of these contributions is 0,085 μGal, which is rounded up to 0,1 μGal. Note that the effects are not necessarily correlated in sign, although the magnitudes of all these effects scale with pressure. Thus the sum of these contributions is a conservative estimate.

6.2 Differential temperature

The existence of a thermal gradient will introduce a pressure gradient across the mass, through the ideal gas law. Simple differentiation of the ideal gas law yields

$$\Delta P = \frac{\Delta T}{T} P.$$

Assuming that the pressure gradient acts directly on the ends of the dropped mass, at a nominal pressure of

$1,3 \times 10^{-4}$ Pa and a temperature of 300 K, the acceleration experienced is

$$a = \frac{\Delta TPA}{TM},$$

yielding a coefficient of 0,40 µGal/°C. Since a temperature gradient across the dropped object decays with time, this eventually yields a negligible acceleration.

The decay time can be estimated using a highly simplified model of the dropped object as a solid rod with a cross-section diameter of 2 cm and a length of 10 cm. If a temperature pulse is applied at one end, the temperature field $T(x,t)$ is described by the diffusion equation

$$T(x,t) = \Delta T \text{erfc}\left(\frac{x}{2\sqrt{\eta t}}\right),$$

where ΔT is the initial temperature difference.

The diffusivity η of aluminium is 0,826 cm$^2 \cdot$ s^{-1} and that of glass is 0,0057 cm$^2 \cdot$ s^{-1}. The dropped object is composed of both aluminium and glass, so we assume the effective diffusivity of the dropped object is roughly 15 % of aluminum, or 0,05 cm$^2 \cdot$ s^{-1}. Evaluating the argument of the complementary error function yields $22 \text{s}^{1/2}/\sqrt{t}$.

A 10 °C temperature difference will introduce a 4 µGal error, but this difference will decay to 1 °C in about 4 minutes and to 0,1 °C in about 40 minutes. A 0,1 °C temperature difference introduces a 0,04 µGal problem. Temperature shocks are most often introduced when the instrument is brought to a new site.

Simple empirical experiments have been conducted to obtain rough operational rules for the instrument. The dropping chamber was heated for 12 hours at a temperature approximately 10 °C above ambient, and then the heating elements were turned off and gravity observations were collected. This experiment attempted to simulate conditions in which the system is transported in a warm vehicle and then deployed at a colder site. No anomalous drift or signal was observed over the next 24 hours. The tentative conclusion is that the system is resistant to thermal shocks. However, one should avoid large thermal changes to the FG5 whenever possible, or allow time for thermal equilibration.

6.3 Magnetic field gradients

A nonuniform magnetic field will induce eddy currents in the electrically conductive dropped object. The eddy currents in turn interact with the field to exert decelerating forces on the dropped object. In the FG5 magnetic fields surround the ion pump, servo motor and Faraday isolator, and could exert significant forces and corresponding errors in the measurement.

We model the problem as an aluminium ring falling

in the field of a point dipole located at the origin of the chosen coordinate system. The plane of the ring is horizontal and the dipole moment is oriented vertically. The effective resistance of the ring is R, and its area is A.

The EMF, E, induced in the ring is simply the time rate of change of the magnetic flux, or

$$E = -\frac{d\Phi_b}{dt} = -\frac{d\Phi_b}{dz} \cdot \frac{dz}{dt} = v \frac{d\Phi_b}{dz},$$

using a velocity $v \equiv dz/dt$. Ohm's law gives the associated induced current I as

$$I = \frac{E}{R} = \frac{v}{R} \frac{\partial}{\partial z} \int_s \vec{B} \bullet \vec{d}A = \frac{v}{R} \int_s \frac{\partial B_z}{\partial z} dx dy.$$

The force acting on the ring is the cross product of the current elements with the magnetic field:

$$F = I \int dl \times B = I \int_s (dA \times A) \times B = I \int \Delta B_z dx dy$$

and the decelerating force of interest is the vertical component F_z

$$F_z = I \int \frac{\partial B_z}{\partial z} dx dy.$$

Substituting for I in the above expression we obtain

$$F_z = \frac{v}{R}\left[\int_s \frac{\partial B_z}{\partial z} dx dy\right]^2.$$

The worst-case force is limited by approximating the above integral as

$$F_z \leq \frac{v}{R}\left(\frac{\partial B_z}{\partial z}\right)^2_{max} A^2.$$

To complete the analysis, an expression for the magnetic field must be derived. A point dipole, of moment m, located at the origin and oriented vertically produces a magnetic field

$$B(r) = \frac{\mu_0 m}{4\pi r^3}\left[3\left(\hat{k} \bullet \hat{r}\right)\hat{r} - \hat{k}\right],$$

where r is a radial vector, k is a circumferential vector and the caret ($^$) denotes a unit vector.

If the field at some reference point z_0 on the z axis is B_0, the dipole moment can be eliminated from the magnetic field expression

$$B(r) = \left(\frac{B_0^3}{2}\right)\frac{\left[3\left(\hat{k} \bullet \hat{r}\right) - \hat{k}\right]}{r^3}.$$

The vertical gradient of the vertical component of B is thus

168

$$\frac{\partial B_z}{\partial z} = \frac{9}{2} B_0 z_0^3 \left[1 - \frac{5}{3} \left(\frac{z}{r} \right)^2 \right] \frac{z}{r^5}.$$

Hence, substituting this expression in the equation for the vertically directed force on the ring yields

$$F_z \leq \frac{v}{R} \left\{ A \frac{9}{2} B_0 z_0^3 \left[1 - \frac{5}{3} \left(\frac{z}{r} \right)^2 \right] \frac{z}{r^5} \right\}^2.$$

For the FG5 system, $v_{max} = 2$ m/s, $B_0 = 1$ mT, $z_0 = 0{,}04$ m, and z_{min} and r_{min} are 0,1 m and 0,18 m, respectively. The diameter, height and thickness of the aluminium cylinder housing the corner cube are 0,015 m, 0,05 m and 0,001 m. The estimated resistance of this "ring" is 0,25 Ω. With these values for the parameters, the force is

$$F_z \leq 1{,}3 \times 10^{-15} \, \text{N}.$$

The mass of the falling body is 0,13 kg, and thus the acceleration a on the body is

$$a \leq 10^{-14} \, \text{m/s} = 10^{-6} \, \mu\text{Gal}.$$

This perturbation is quite insignificant. A serious objection to this calculation is that certain parameter choices such as the equivalent resistance and effective ring thickness are arbitrary. However, the parameters can be adjusted upwards a great deal and still generate a negligible force on the dropped object. Note that the effect is inversely proportional to the effective ring resistance and scales as the square of the field magnitude. A fortuitous property is the rapid decrease of the force with distance from the dipole source.

It is difficult to actually measure induced currents in the dropped object. Note that the error signal is dependent on the local magnetic field gradient. Observed fields near the dropped object are of the same magnitude as the Earth's magnetic field, 50 μT. The measured fields of the ion pump magnet, servo motor and Faraday optical isolators are less than the Earth's field at the dropped location of the object.

To test the sensitivity of the FG5 to eddy current forces, magnetic fields of order 100 μT were applied to the system with a set of Helmholtz coils, operated to generate rather than cancel local fields. The coil location was such that the field gradient was intentionally at a maximum. Figure 6 presents the results of the experiment; no changes in the observed value of g at the 1 μGal level were seen with different applied fields. Given both the calculated and experimental results, the instrument uncertainty attributed to magnetic fields is 0,1 μGal.
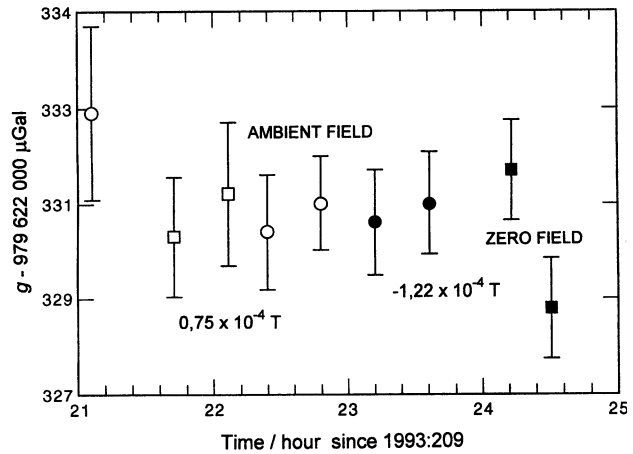

Figure 6. Observed gravity values as a function of applied magnetic fields. The data are corrected for environmental signals.

6.4 Electrostatics

One model of electrostatic attraction pictures the dropped object and the co-falling chamber as two halves of a capacitor that is charged by the thermal EMF of the contact points: this thermocouple effect generates a voltage at the tungsten-aluminium interface.

The mass and carriage cross-sections are circular, with a radius of 15 mm and separation of 1 mm at rest, so the equivalent capacitance is

$$C = \varepsilon_0 \frac{A}{d}$$
$$= 6{,}3 \, \text{pF}.$$

The thermal EMF acts as a battery that charges the "capacitor" during the hold phase. During the mass release, the circuit is opened, disconnecting the battery from the capacitor. As a very conservative example, the junction is modelled as a type E thermocouple (nickel-10 % chromium in contact with constantan). The sensitivity of such a junction is 61 μV/°C.

If we assume a temperature of 30 °C, the associated thermal EMF is only 1,8 mV. The charge on the capacitor is thus

$$q = CV = 1{,}2 \times 10^{-14} \, C.$$

The force between the capacitor plates can thus be evaluated as

$$F = \frac{q^2}{2\varepsilon_0 A} = 1{,}0 \times 10^{-14} \, \text{N}.$$

The associated acceleration is minuscule, for a 0,1 kg mass, it is of order 10^{-5} μGal.

One particular concern is the development of patch charges on the co-falling chamber and dropped object. For this reason all elements of the dropped object and surrounding cart are conductive. Even so, the surfaces of the objects still contain thin layers of aluminium oxide, which can support patch charge formation. In this case the electrostatic force could then change with time as the patch charges migrate. It is difficult, however, to produce as much patch charge as was calculated above using the simple thermocouple model.

The attraction due to electrostatics is highly sensitive to the distance between the falling test mass and the co-falling chamber. Tests have been conducted in which the separation was varied between two extremes, changing the separation by a factor of 4. Results show that any electrostatic effects are less than 1 µGal, the nominal measurement uncertainty. Since the electrostatic force should scale as the inverse square of the separation, this experiment is consistent with our 0,1 µGal error assessment.

6.5 Attraction of apparatus/environmental mass changes

The attraction of the apparatus has been considered as an error term in previous error budgets, but as it can be calculated to arbitrary accuracy it should really be treated as a simple correction rather than an error. There is some worry that nearby mass fluctuations (even the mass of an operator) can cause significant gravity fluctuations.

A figure of merit to note is that a 0,1 µGal signal can be generated by a 1 kg mass at a range of 25 cm, or 10 kg at a range of 81 cm directly above or below the gravimeter. It is unlikely that such a 1 kg mass would be overlooked, and thus a figure of 0,1 µGal is assigned to this type of error.

Clearly, it is important that users remain aware of potential mass changes such as new buildings, snow, water table changes or even deforestation during epoch measurements at any given site.

6.6 Verticality

Operator errors in setup are the primary source of verticality errors. The fractional error in g is a cosine term, approximated for small angles by

$$\frac{\Delta g}{g} = -\frac{\theta^2}{2},$$

where θ is the alignment error. The T2 telescope used in the FG5 system resolves 5 µrad, and it is possible to collimate the vertical reference beam with respect to a beam reflected from a level pool by 1/3 of the apparent

beam diameter, or 24 µrad. The optical system used provides an optical magnification of 2 in the beam angular deflection, thus providing a total angular resolution of 12 µrad. This gives a fractional error of 7×10^{-10} or 0,07 µGal.

Sites with high levels of seismic noise introduce vibrations in the alcohol pool and make alignment rather difficult. As a result, the error can be higher. Fluids with somewhat higher viscosity, such as silicone oils, can be used if the edge of the fluid meniscus is avoided.

An additional verticality bias associated with the vacuum window has been discussed by Zumberge [16]. The beam path travels through three different optical media: glass, air and vacuum. Even if the vacuum port is absolutely plane parallel, the beam is deflected from the vertical by an amount

$$\Delta \theta = (n_a - 1)\theta,$$

where θ is the incidence angle of the beam with respect to the vacuum window. The vacuum window is deliberately tipped 0,5° in order to avoid direct reflections so the verticality bias is 2,6 µrad and introduces an error of 0,034 µGal. The uncertainties due to setup errors and the tilt of the vacuum window are estimated to total 0,1 µGal.

6.7 Air gap modulation

Since the FG5 interferometer is not evacuated, it is subject to another source of optical path length perturbations known as air-gap modulation [24]. Vibrations of the dropping chamber translate the optical window of the dropping chamber, which is the interface between air and vacuum. If the dropping chamber is displaced by an amount x, the path length changes by $(n_a - 1)x$, where n_a is the index of refraction for air (nominally 1,0003). Observed translations x are sinusoidal with amplitudes of 1 µm to 2 µm. The perturbations are highly reproducible from drop to drop and thus introduce a systematic gravity bias. The gravity bias depends strongly on the frequency, amplitude and especially the phase of the oscillation.

The in-line interferometer does not compensate for air-gap modulation. Possible solutions include decreasing the dropping chamber recoil, shifting the recoil frequency to high frequency or placing the entire optical path in vacuum. We considered designs that evacuate the optical path but all introduce a mechanical connection between the dropping chamber and the interferometer-Super Spring assembly. The effect of directly coupling vibrations between these subsystems is difficult to minimize and characterize. Furthermore, the system is significantly easier to use if the interferometer is not evacuated.

We chose instead to mitigate the vertical oscillations

Table 1. Laser uncertainty.

Error component	Quoted error coefficient	Measurement error	Estimated frequency error
Polarization-stabilized laser			
Frequency drift	5 MHz/year	3 month calibration	1,6 MHz
Temperature dependence	0,3 MHz/°C	0,5 °C	0,15 MHz
Air pressure	7 MHz/MPa	0,04 MPa world-wide	0,28 MHz
RMS frequency error			1,6 MHz
Associated gravity error			3,4 µGal

Error component	Fractional stability	Uncertainty	Gravity error
Iodine-stabilized laser			
Absolute accuracy	2×10^{-10}	0,1 MHz	0,2 µGal
Repeatability (long-term)	2×10^{-11}	0,01 MHz	0,02 µGal
Alan variance (1000 s)	3×10^{-13}	142 Hz	0,00015 µGal
Associated gravity error			0,2 µGal

of the dropping chamber by refining the mechanical design. Studies showed that the tripod legs flex radially outward like tuning forks during the drop. Fluoropolymer sheets, specifically designed for vibration damping, were inserted in the joint between the dropping chamber support tripod and the tripod legs, and also under the tripod feet. The pads quickly damp out the tripod vibrations and reduce the portion of the drop contaminated by vibrations. The pads are compliant and also serve as a weak adhesive to fix the tripod to the floor. The tripod foot design was changed from balls set in radially oriented vees to balls set in cones; this design is overconstrained kinematically, but constrains radial flexing. Another significant vibration source was found in the oscillations of the dropping chamber guide rod assembly, along which the co-falling carriage rides. Locking screws now hold the rod assembly against the vacuum chamber walls, dramatically increasing the structure's rigidity.

A numerical modelling approach to correcting the path length perturbation was described by Klopping et al. [25]. By carrying out a spectral analysis of the cumulative residuals over many drops (of order 1000), statistically significant spectral components are identified. The components are then iteratively removed from the original data, and the original bias computed. This numerical analysis was applied to data from the prototype FG5 system and initially indicated biases of order 5 µGal or more.

6.8 Laser wavelength (length standard)

The *g* value obtained depends directly on the wavelength or frequency of the laser. If the true optical frequency is higher than the value used in calculations, the error in *g* scales linearly as 2,07 µGal/MHz. As discussed in Sec-

tion 2, the FG5 gravimeters employ two types of laser, frequency-stabilized by different techniques. The preferred device is the iodine-stabilized laser, as it is a primary wavelength standard and does not require calibration. The uncertainty budget for these two lasers is given in Table 1. The frequency drift figure given for polarization stabilized lasers is quite pessimistic, as the drift rate is linear and interpolation can be used to correct the wavelength between calibrations. We have assigned nominal uncertainties of 3,4 µGal for data collected with polarization stabilized lasers and an uncertainty of 0,2 µGal for data from iodine-stabilized lasers.

Despite the distinct metrological advantages of iodine-stabilized lasers, the polarization-stabilized lasers can be usefully employed. These lasers require careful operation and frequent recalibration, but are more rugged and robust.

6.8.1 Diffraction limit

The spatial filter and collimation assembly used in the FG5 system introduce a finite curvature in the collimated beam wavefronts, that changes the effective wavelength of the interferometer. This effect can be calculated from measurements of the beam waist, and is given by [26] as

$$\frac{\Delta \lambda}{\lambda} = \left(\frac{\lambda}{2 \pi w} \right)^2 ,$$

where the beam waist *w* is of order $(2,25 \pm 0,05)$ mm, and the related gravity correction is of order 2 µGal.

The uncertainty in *g* is directly related to the fractional uncertainty in the diffraction correction, or

$$\frac{\Delta g}{g} = \frac{\lambda}{\pi w} \frac{\Delta w}{w} .$$

The uncertainty in the beam waist results in an uncertainty in the diffraction correction of 0,2 µGal.

Historically many gravity observations have not been corrected for this effect because it has been below the stated accuracy. At our current level of accuracy, however, we must include the correction for proper intercomparison with other instruments.

6.8.2 Beam shear

The corner-cube design is inherently insensitive to beam translation and rotation in the idealized case of plane wave interferometer beams. The in-line interferometer extends this property to the entire optical path. The two interfering beams can, however, be translated relative to one another: this occurrence is termed beam shear. Beam shear can be introduced by motion of the interferometer base or corner cubes, especially translations of the falling corner cube. As discussed in Section 6.10, typical translational velocities are of order $1,5 \times 10^{-4}$ m/s for a drop time of 0,2 s, giving rise to a horizontal beam shear of 3×10^{-5} mm. Assuming that the phase distortion across a non-plane wave beam is of order $\lambda/10$ and the beam diameter is $6 \text{ m} \times 10^{-3}$ m, we find a differential phase shift

$$\Delta\phi = \frac{\lambda}{10} \frac{3 \times 10^{-5} \text{ m}}{6 \times 10^{-3} \text{ m}} = 1,5 \times 10^{-10} \text{ m}.$$

The fractional error in gravity is roughly proportional to the fractional error in the distance measurement so that for a drop length of 0,2 m we have a gravity error of 0,8 µGal. This calculation is an overestimate because the beam shear error would mimic a velocity term if the spatial phase varies linearly, and would not perturb the gravity determination. Other motions such as recoil of the floor, acoustic vibrations in the interferometer or seismic noise could also introduce beam shear contributions. We are currently calculating more realistic beam shear models.

6.9 Corner cube rotation

Optical path length errors are created by rotation of the object during the drop. We suspect that rotation of the object is caused by flexing of the co-falling chamber as the test mass is released, rather reminiscent of a diving board. The path length change due to rotation of a corner cube is simply given by considering the motion of the optical centre [27]. This result is strictly valid for open corner cubes. The result is approximately valid for glass corner cubes since the deviations from this law are very small (quartic in the angular changes around the optical centre) [28]. For a free-falling test mass, rotations occur around the centre of mass so the problem can be mini-

mized by balancing the corner cube at the optical centre. In practice there is always a residual deviation, ε, between the centre of mass and the optical centre due to imperfect balancing. The change in apparent vertical position is at a maximum when ε is horizontally oriented since the optical centre position varies as the sine of the rotation angle. Fortunately, this position error is approximately linear in time for small angles and a constant rotation rate: it thus mimics a change in initial velocity and has only a very small acceleration component. More problematic is the effect that occurs if the deviation, ε, between the optical centre and centre of mass is vertical. Then the apparent position resembles a cosine error which has a parabolic component that mimics a gravity signal. The vertical path length error is given by

$$\Delta z = [1 - \cos(\omega t)]\varepsilon$$
$$\approx -\varepsilon\omega^2 t^2/2,$$

where ω is the rotational velocity. The apparent acceleration is $\varepsilon\omega^2$. Measured rotation rates are of order 10 mrad/s and the uncertainty in locating the optical centre and centre of mass is $2,5 \times 10^{-5}$ m. Thus, the expected uncertainty is about 0,25 µGal.

The dropped object rotation can be observed and recorded during each drop with an optical system. This system reflects a laser beam from a mirror on the top of the dropped object and detects the beam angular displacement with a position sensitive photodetector. Computing rotation corrections is not trivial, as the displacement ε is unknown, but the rotation measurements can be used as a criterion to reject any drops that exceed 10 mrad/s.

The rotation rate may increase with time, as the kinematic mount between the test mass and the co-falling carriage wears with use. The kinematic mount is a set of three balls in the test mass that rest on three radial vee-grooves on the carriage. The rotation rate must be carefully monitored over time, and the balls and vees replaced as necessary.

6.10 Coriolis effect and translations of the dropped object

Translations of the dropped object in the east-west direction give rise to a Coriolis acceleration in the vertical plane with a magnitude

$$a_c = 2\Omega_e v_{E-W} \sin(\theta) = \frac{14,5 \text{ µGal}}{\text{mm/s}} v_{E-W} \sin(\theta),$$

where Ω_e is the Earth's rotational rate, v_{E-W} is the east-west component of the velocity and θ is the co-latitude of the observation. Measurements of the horizontal translation velocities are of order 0,15 mm/s to 0,20 mm/s, yielding worst-case errors of 2 µGal to 3 µGal. The worst-case errors occur at the equator, with velocities

parallel to the east-west axis. Typically, the translation of the dropped object is systematic and oriented roughly perpendicular to the drive-belt axis. It is likely that the magnitude and direction vary somewhat from system to system and with operating conditions.

If the carriage is aligned so that the repeatable translation vector is in a north-south line, the Coriolis effect can be reduced. With the velocity vector aligned to within 10° of the north-south line, the worst-case error is 0,5 μGal.

Currently the best approach is to align the translation vector along a north-south line and then measure the velocity and subtract the error term. Using very simple detectors, this can be done to about 10 % and reduces this error below 0,33 μGal at all latitudes and orientations of the instrument. Currently efforts at the BIPM aim to reduce this translation by stiffening or balancing the drive system.

6.11 Floor recoil and tilt

The issue of tilt is essentially eliminated by the design of the in-line interferometer, but a related effect still exists. The floor or platform supporting the system recoils upwards when the test mass is released. The deflection of a square plate clamped at the edges is given by

$$\delta z = \frac{Fl^2}{4Et^3}.$$

Evaluating this expression for a force F of 10N, a length l of 2 m, thickness t of 0,12 m and an elastic modulus E of 6×10^{10} Pa, yields a maximum displacement of 12 nm. Note that this is far smaller than the recoil response of the instrument itself.

The Super Spring is isolated from the floor recoil and the test mass is in free fall, so the physical displacement of the floor generates an optical path length change identical to the air-gap modulation problem. The optical path length change is of order 4×10^{-12} m. If the time behaviour of the floor recoil exactly followed a parabola, the bias in g would be 0,02 μGal. Note that a sensible site would be a ground-floor room supported at the base. The total error for this effect is negligible.

However, there is an unresolved recoil issue. The inertial mass in the Super Spring is not perfectly isolated and will track the floor recoil to some extent. The isolation of the new Super Spring has not yet been rigorously evaluated but these tests are under way.

6.12 Electronic phase shift

Frequency-dependent time delays in the photodetector and voltage comparator can introduce phase shifts that resemble velocities and accelerations in a least-squares

fit to the trajectory. In particular, the high-pass filter (an RC network used for ac-coupling) and the upper corner frequency of the photodetector circuit introduces a bias in g. The upper-corner frequency, modelled by a single pole, has the useful property that a first-order phase shift mimics a velocity term. The lower-corner frequency of the RC network high-pass filter introduces a phase shift that mimics gravity. Analytic continuous least-squares estimation [22] and numerical simulations for the response of a simple one-pole filter have been used to estimate the measurement bias. For the RC high-pass filter component values of 4,7 μF and 50 Ω, the correction is of order 1,4 μGal. Variations in the filter corner frequency are due to component variations, the least controlled of which are capacitors, nominally 10 %. Thus, uncertainties in the filter model correction are of order 0,14 μGal. A new detection circuit is being designed with greater bandwidth that should significantly reduce these problems.

One of the most critical elements in the measurement is the high-speed comparator (discriminator) that converts the zero-crossings of the sinusoidal fringe signal to a TTL square wave edge suitable for timing measurements.

A constant delay time between the actual zero-crossing and the TTL edge does not affect gravity measurements but dispersion of the delay time as a function of the frequency of the input fringe signal can mimic a false gravity signal. It is important to keep the frequency dependent part of the time delay less than 32ps/MHz in order to keep the associated error below 1 μGal [22].

It is customary to describe this dispersion as a time delay that depends on the slew-rate or the speed through which the sinusoidal signal crosses zero. For a frequency, ω, and amplitude, A, the slew rate is proportional to the product $A\omega$. At high slew rates (larger amplitude and/or higher frequency) the time delay is typically smaller than for low slew rates (lower amplitude and/or lower frequency). Since our measurement requires a signal which sweeps from a few hundred kilohertz to about 6 MHz it is important to have a large amplitude so that the slew rate is always acceptable.

The JILAg and FG5 gravimeters used a comparator called an AMD686 (686). These 686 comparators have a nominal 12 ns delay time. The frequency-dependent time delay was measured at the JILA in 1987 [22] and was determined to contribute less than 0,6 μGal error to the measurement.

Discrepancies in the 1994 BIPM intercomparison led us to make further measurements of these time delays and we have found that the errors increase dramatically at low fringe amplitudes (low light levels). These effects were noticeable in the BIPM intercomparison because different groups used different light levels and several lasers on the systems suffered from rapidly ageing laser tubes. Subsequent measurements made by the NOAA

Table 2. Comparator test.

Fringe signal/mV	Gravity/µGal		Correction/µGal	
	686	9696	686	9696
44,7		468,8		9,8
50,1		466,4		9,4
56,2	474,9	466,7	17,9	9,7
63,1	473,6	465,9	16,6	8,9
70,8	473,1	463,9	16,1	6,9
79,4	472,4	462,7	15,4	5,7
89,1	471,9	461,2	14,9	4,2
100,0	471,3	460,0	14,3	3,0
112,2	470,7	459,1	13,7	2,1
125,9	470,6	457,9	13,6	0,9
141,3	470,8	457,3	13,8	0,3
158,5	471,1	456,7	14,1	−0,3
177,8	470,6	456,5	13,6	−0,5
199,5	470,0	456,5	13,0	−0,5
223,9	468,2	456,5	11,2	−0,5
251,2	466,2	456,6	9,2	−0,4
281,8	463,9	457,0	6,9	0,0
316,2	461,9	456,9	4,9	−0,1
354,8	459,9	457,0	2,9	0
398,1	458,1	457,0	1,1	0
446,7	456,7	457,1	−0,3	0,1
501,2	456,0	457,1	−1,0	0,1
562,3	455,9	457,1	−1,1	0,1
631,0	455,9	457,2	−1,1	0,2
707,9	456,6	457,1	−0,4	0,1
794,3	457,0	457,0	0	0
891,3	457,5	457,1	0,5	0,1
1000,0	458,2	456,9	1,2	−0,1

group at Table Mountain indicate that low light levels could indeed cause changes in the gravity value. We also found that when we used a newer and much faster comparator, called an AD9696 (9696), the gravity value varied less with changing light level. Moreover, the gravity values obtained from the two comparators agreed at higher light levels.

To test this effect more systematically, the NOAA group at Table Mountain built a test apparatus consisting of a very stable function generator (HP3325B) with an rf-attenuator circuit on the output, a box that can hold two detector boards, and the standard timing electronics and gravity processing software used in the FG5. The function generator produced a frequency-swept sinusoid to simulate our fringe signal after the avalanche photodiode. The rf-attenuator was used to reduce the amplitude in discrete reproducible steps. The comparator converted the zero-crossings for the FG5 timing electronics and data analysis software. By swapping input cables the two comparators (686 and 9696) could be tested relative to one another. The output of this test is a simulated gravity value.

The data are shown both in Table 2 and Figure 7. The gravity value has an arbitrary offset of 457 µGal but changes are clearly evident at low fringe amplitudes for both comparators. The 686 comparator agrees with the
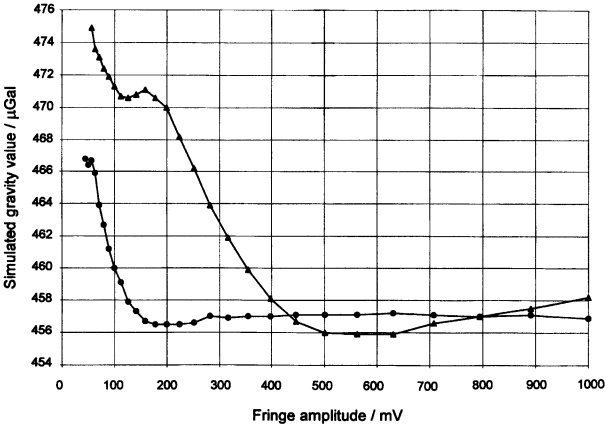

Figure 7. Errors from two different comparators as a function of input fringe signal amplitude. ▲ 686; ● 9696.

9696 above about 400 mV to about ± 1 µGal. Below this level the 686 has a steep dependence on the fringe amplitude. By comparison the 9696 is very flat (± 0,2 µGal) above 280 mV fringe amplitude.

Corrections based on these curves have been applied to the BIPM intercomparison and to measurements taken

Table 3. FRK-L rubidium frequency standard uncertainty budget.

Error component	Quoted error coefficient	Estimated variation	$10^{10} \times$ fractional frequency uncertainty
Drift	4×10^{-11}/month	4/month	1,6
Retrace	2×10^{-11}	N/A	0,2
Supply voltage	10^{-11}/10 % variation	10 %	0,1
Operating temperature	3×10^{-10} from -25 °C to 65 °C	20 °C	0,6
Magnetic field	3×10^{-7}/T	2×10^{-4} T	0,6
Altitude	10^{-9}/MPa	0,03 MPa	0,3
Frequency uncertainty (root sum squared)	$3,4 \times 10^{-10}$		
Associated gravity uncertainty contribution	0,6 µGal		

at the TMGO. These corrected gravity values improve the agreement between instruments.

In addition to tests on the comparator, we have made a different detector with a PIN diode (instead of an avalanche photodiode) and a fast amplifier. The new detector also has the possibility of lowering the corner-frequency of the high-pass (ac-couple) filter to 1/2 Hz. Tests with these new detectors agree with the older detectors made with avalanche photodiodes at the 1 µGal level. This increases our confidence that we do not have problems in the optical detector or in the ac-couple circuitry. These new circuits have decreased the single drop scatter to as low as 4 µGal and the residual noise for a single drop to as low as 0,5 nm.

We are still testing the effects of frequency-dependent time delays and building different detectors with different amplifiers, filters and comparators. At the moment our best estimate of the error due to timing electronics is below 0,6 µGal as long as the 9696 comparator is used above a fringe level of 300 mV.

6.13 Rubidium frequency reference (time base)

The rubidium frequency reference used is the Efratom FRK-L model; manufacturer specifications for fractional frequency accuracy are listed in Table 3 [29]. A pessimistic error estimate for the Rb standard is 0,6 µGal, assuming the worst-case drift rate and a four-month recalibration schedule.

The largest error contribution is due to drift, which can be controlled by frequent calibrations against caesium beam standards (direct or transferred). Actual operating experience indicates that, with frequent recalibration, a Rb standard can be maintained at 1 part in 10^{10}, yielding a gravity uncertainty of 0,2 µGal; this is the assigned uncertainty contribution.

6.14 Glass wedges

Figure 4 shows the method used to align the beam so that it is vertical. The beam splitters, optical vacuum windows, compensator plates and attenuator plates are all specified as plane parallel optical flats. The alignment procedure steers the test and reference beams into mutual parallelism, and thus ensures beam verticality. Beam deflections due to wedges introduce a bias when setting the alignment, even when the test and reference beams are parallel.

The beam geometry is straightforward but tedious, and each case must be considered: air-glass-air and air-glass-vacuum as well as angle of incidence from zero to 45°. All the expressions are linear in terms of the wedge angle. These angular deviations are below 25 µrad if optical flats with 1 arc sec parallelism specifications are used in the critical path; this is especially critical for the attenuator plate because of the multiple reflections employed. The combined effects give an estimated uncertainty of 0,3 µGal.

6.15 Radiation pressure

For a photon of energy $h\nu$, the momentum transfer for total reflection is $2 h\nu/c$. Thus, for a laser of power P, the total momentum transfer is simply $2 P/c$. For a 100 mW laser, the force on the dropped object is 7×10^{-12} N, and contributes an acceleration of less than 0,01 µGal.

6.16 Uncertainty budget summary

The uncertainty sources are summarized in Table 4. By simple inspection most terms are uncorrelated. Many of the sources, such as temperature gradients or electrostat-

Table 4. FG5 uncertainty budget estimate.

Error source	Uncertainty/μGal	Comments
Residual air pressure	0,1	Pressure-dependent
Differential temperature	0,1	Temperature- and pressure-dependent
Magnetic field gradient	0,1	Difficult to estimate
Electrostatics	0,1	Difficult to estimate
Attraction of apparatus	0,1	Fixed bias in instrument design
Verticality	0,1	Operator-dependent, always negative
Air gap modulation	0,6	Setup-dependent
Laser wavelength	0,1	Iodine-stabilized laser only
Corner-cube rotation	0,3	Can degrade with time
Coriolis effect	0,4	Strong latitude and setup dependence
Floor recoil and tilt	0,1	Site-dependent
Electronic phase shift	0,6	
Frequency standard	0,2	
Glass wedges	0,3	
Diffraction limit	0,2	Laser system-dependent
Total uncertainty	1,1	RSS uncertainty estimate

Table 5. Uncertainties in determining environmental sources terms of gravity.

Source	Signal range /μGal	Signal removal uncertainty/μGal	Time scale
Solid Earth tides	300	0,2-0,5	Diurnal
Equilibrium ocean loading	20	0,2	Diurnal
Tidal swell and surge	19	5	Minutes
Atmospheric attraction and loading	8	1-5	Hours-Diurnal
Water-table variations	Site-dependent	Site-dependent	Seasonal
Polar motion	10	< 0,01	12, 14 months
Microseisms	0-20	0	< 100 Hz

ics, are also random processes. The instrumental uncertainty estimate explicitly assumes that these terms are uncorrelated. The corresponding overall uncertainty given by the square root of the sum of the squares of the individual uncertainty estimates is 1,1 μGal.

Many of the largest terms in the uncertainty budget arise from the effects of recoil and of imperfections in the dropping mechanism. Current efforts to stiffen the tripod and dropping mechanisms may further improve the instrument. More work, necessary to improve the rise and fall capability of the FG5, could potentially reduce the 0,6 μGal error due to frequency-dependent phase shifts. On the other hand, the more problematic errors caused by recoil, rotation, air gap modulation, and translation of the object would be increased if a rise and fall trajectory were used, because the system recoil is greater during the throw portion of the trajectory.

6.17 Environmental signals

The uncertainty sources described in the previous sections relate only to the acceleration measurement itself. Variations in the observed values of gravity arise from a combination of both instrumental artefacts and real gravity signals. Some of the environmental signals can be large and they are difficult to model. It is arguable that an instrumental accuracy of 1 μGal is sufficient given the difficulty in modelling the environment to this degree of accuracy.

Signals from geological sources, such as tectonic deformation or volcanism, range in period from years to aeons. Other signals vary at higher frequencies, ranging from minutes to years. Such signals include the tidal accelerations of the Sun and Moon [30, 31], ocean-loading effects [32], variations in the water table, atmospheric attraction and loading effects [33, 34], polar motion [35], and microseismic signals [36]. These signals are often referred to as environmental gravity signals; Table 5 lists these signals. For most applications, water table variations are of the greatest concern. For large underground reservoirs, the gravitational attraction of the water table can be modelled by an infinite plane of water (42 μGal/m) scaled by the bulk porosity. Bulk porosities vary from < 3 % in competent granite to greater than 50 % in sands. Well records can resolve water table variations of a few millimetres and easily provide correction data at the level of a few microgal, if the local water

table is spatially homogeneous. Conversely, gravity changes at the level of a few microgal can be used to detect large-scale ground water changes.

Microseismic signals range in period from 100 s to 0,01 s (100 Hz), with amplitudes of order 10^{-6} m; Aki and Richards [36] present characteristic spectra. Naturally occurring microseismic noise has poor phase coherence and can be treated as random noise in the gravity data. The effect of microseismic noise averages to zero with a sufficiently large sample. In general, artificially generated vibrations dominate any given site and should be eliminated or avoided for minimum observational noise. Teleseismic signatures of distant earthquakes generate tremendous acceleration noise, but are fortunately infrequent. These signatures are easily seen in the gravity time series, the Super Spring trace, and they can be verified by data from seismometer networks.

Environmental signals are not part of the uncertainty estimate for any absolute gravimeter. The signal sources generate real gravitational accelerations and would be observed by a perfect gravimeter. The problem of extracting a mean or epochal gravity value is one of signal discrimination rather than instrumental design.

7. Observational results

Results from the FG5 system indicate that the initial design goals have been met. The series of instrument tests and assessments also confirms conformity with the design goals, as shown in the uncertainty budget.

Several experiments have been made with two FG5 gravimeters running simultaneously in one room. In these, gravimeter locations were switched and gravity was measured again. This differential experiment removes both environmental gravity signals and horizontal gradients. In one experiment locations were swapped twice and four different measurement sets were obtained. The result was a differential acceleration of 0,94 µGal with a standard deviation of the mean of 1,0 µGal.

An on-going instrument intracomparison is being conducted at the National Oceanic and Atmospheric Administration (NOAA) Table Mountain facility using a majority of the FG5 gravimeters that have so far been constructed [37]. The measurements consist of simultaneous (or nearly simultaneous) runs of different FG5 gravimeters with one of the two NOAA gravimeters (JILAg-4 and FG5-102). Figure 8 shows the data from different gravimeters over time. The standard deviation of the mean of observations with all instruments is 1,8 µGal, in agreement with the instrumental uncertainty estimate. Notice that during the first year the formal uncertainty estimates and measurement deviations are considerably larger than in the second year. The earlier versions of the instruments did not use iodine-stabilized lasers or have all the mechanical modifications which reduce the air-gap modulation problem. For data col-
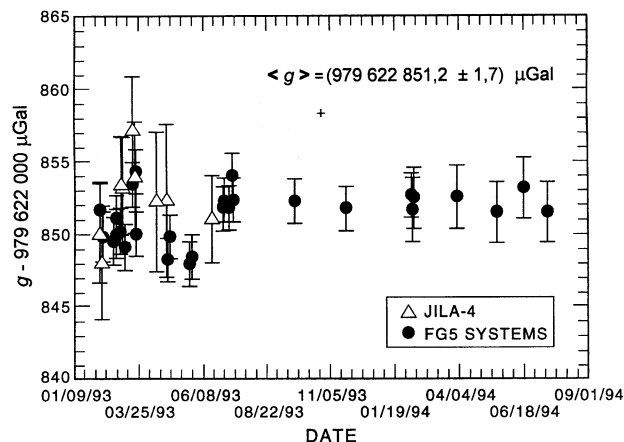

Figure 8. Results from the Table Mountain Intracomparison. FG5 systems 101, 102, 103, 106, 107, 108 and JILAg-4 are presented. (Reprinted from Sasagawa et al. [37].)
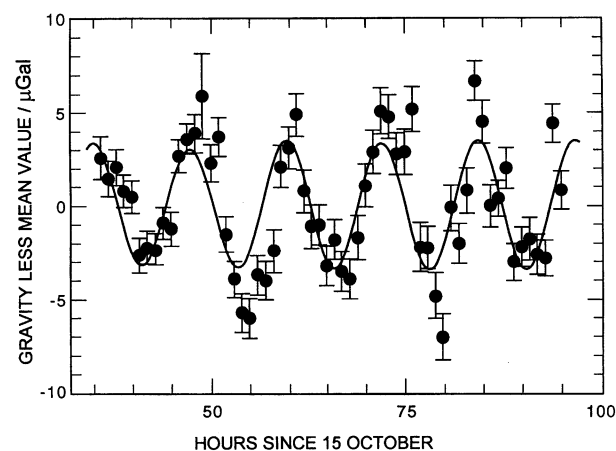

Figure 9. Data collected at the BIPM. Note how the data track the predicted ocean-loading response.

lected from 30 June 1993, the standard deviation is 0,7 µGal. Also note the general agreement between the JILAg and FG5 series of gravimeters.

Figure 9 presents initial data taken with FG5-108 at the BIPM. They have been corrected for Earth tides and local air pressure but not for the effect of ocean loads. The ocean-load model is also plotted. The gravimeter clearly tracks the ocean-load signal of about 6 µGal.

An important characteristic of absolute gravimeters is that their accuracy is constant over a wide bandwidth extending down towards dc. There is much evidence from tidal observations that absolute gravimeters perform well over time scales of days. The Table Mountain data presented in Figure 8 show stability at the 1,8 µGal level over a period of several years. This figure explicitly
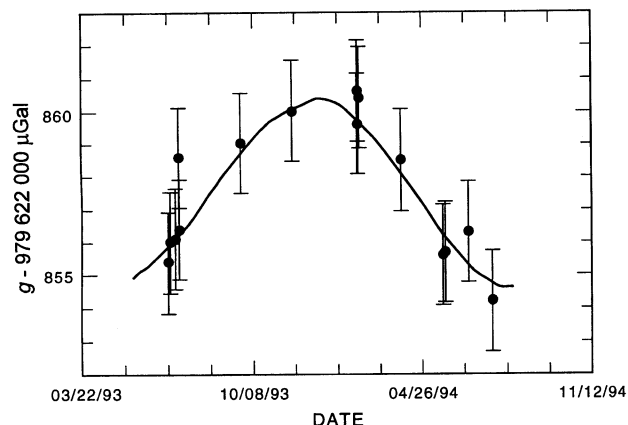
8. Conclusions

Figure 10. Polar motion gravity signal computed from VLBI observations and the gravity signal observed at TMGO, uncorrected for the polar motion. This figure includes data after 30 June 1993.

removes the polar motion signal observed at this site. Figure 10 presents the last year of measurements (June 1993 to July 1994) without a polar motion correction, together with the polar motion signal computed from VLBI data. The RMS deviation from the expected polar motion signal is 0,7 μGal; the maximum deviation is 2,3 μGal over a signal with a peak-to-peak amplitude of 5 μGal.

To our knowledge, this time series is the best absolute gravimeter observation of polar motion to date. The polar motion observed is very similar to that obtained with superconducting relative gravimeters, with one important difference, which is that in the analysis of superconducting gravimeter data a correction must be made for the known polar motion signal in order to obtain an accurate empirical exponential drift function. Absolute gravimeters require no such a priori knowledge or drift term calculations. This difference is crucial when monitoring long-period gravity signals of unknown structure. Another key difference is that the absolute measurements were obtained using more than one instrument, confirming that the results of different instruments from different groups may be combined in an unambiguous fashion.

We are currently working on the design of a new detector with the objective of lowering the noise level and further reducing the frequency-dependent phase errors. Ongoing experiments should make it possible to determine the current limitations of absolute gravimeter technology.

Finally, the FG5 appears to be robust and capable of withstanding long field trips. Actual operational missions have been conducted with the FG5 system. Over a six-week period with operations in Taiwan, Japan and Hawaii [13] no significant breakdowns were encountered. Operational activities have also been conducted by other groups.

The FG5 system incorporates significant design improvements based on an improved understanding of measurement issues in absolute gravimeter design. The associated issues of optical path perturbations and systematic numerical biases have, in the past, been significant problems. The in-line interferometer and tripod assembly directly address this problem. Uncertainties in the laser wavelength have also been effectively eliminated by incorporation of an iodine-stabilized laser. Iodine lasers are not new in design or application to absolute gravimeters, but this laser is far more reliable and robust than previous lasers.

Noise performance has met the original design goals. The new Super Spring improves on the JILA series in both size and operation, while providing comparable performance. The data variance reduction afforded by the Super Spring provides a significant decrease in the total number of drops required for any given precision.

Accuracy improvements have been achieved through the new interferometer design. Other FG5 improvements include vacuum system performance, optical element tolerances and signal transmission. Many changes have improved reliability and ease of use.

Alhough unambiguous accuracy determination is difficult, the uncertainty budget estimate of order 1 μGal is strongly supported by a series of instrument comparisons which are themselves unambiguous tests of instrument precision (though not accuracy).

Individual instrument standard deviations achieve a value of 5 μGal to 8 μGal at quiet stations well removed from human activity. At these sites the JILAg gravimeters and FG5 gravimeters have similar variances. At sites with more noise, the FG5 can be quieter by a factor of 2 to 3. This is consistent with the in-line design which couples less noise into the measurement than the JILAg system.

It is still not known what generates the instrumental noise level of 5 μGal to 8 μGal. The best candidates are incomplete isolation of the Super Spring, noise in the timing measurement, variations in the translation and rotation of the free-falling mass, or interferometer-based noise such as beam shear. Recently we have achieved smaller residual noise (~ 0,8 nm on a single drop) and lower gravity scatter (5 μGal on a single drop) at the Table Mountain site by lowering the bias voltage on the avalanche photodiode detector.

Mechanical designs targeted to reduce rotation and translation of the test mass are also under consideration. The FG5 systems are now deployed in operational programmes and are expected to yield years of service.

Key participants include members of the Axis Instruments Company, the National Institute of Standards and Technology, the National Oceanic and Atmospheric Administration, the Institut für Angewandte Geodäsie and the Bureau International des Poids et Mesures. This work is supported by the NOAA Global Climate Change programme and the NIST Quantum Physics Division.

Note. The mention of commercial products in this paper is for informational use only and does not constitute an endorsement by the US Department of Commerce, NIST, NOAA, or any other agency of the United States government.

Appendix 1

The equation of motion for a test particle free falling in a gravitational field is

$$\ddot{z} = \frac{G \cdot M}{z^2}.$$

The first-order linear approximation of a constant acceleration and a linear gradient term yields

$$\ddot{z} = g_0 + \gamma(z - z_0),$$

where g_0 and z_0 are the initial acceleration and position and γ is the gradient. The general solution for this differential equation is

$$z(t) = z_0 + \frac{g_0}{\gamma}\left[\cosh\left(\sqrt{\gamma}t\right) - 1\right] + \frac{v_0}{\sqrt{\gamma}}\sinh\left(\sqrt{\gamma}t\right),$$

where v_0 is the initial velocity.

A power series expansion of the differential equation provides an alternate solution:

$$z(t) = z_0 + v_0 \sum_{n=0}^{\infty} \frac{\gamma^n t^{2n+1}}{(2n+1)!} + g_0 \sum_{n=0}^{\infty} \frac{\gamma^n t^{2n+2}}{(2n+2)!}.$$

We employ the previous expansion of the equation of motion, truncated to first order in γ. The data are fitted to this equation by linear least-squares methods, assuming a known gradient. The model equation is thus linear in the trajectory parameters (x_0, v_0, g_0)

$$z(t) = z_0 + v_0\left(t + \frac{\gamma}{6}t^3\right) + \tfrac{1}{2}g_0\left(t^2 + \frac{\gamma}{12}t^4\right).$$

The instrument references the observed acceleration to a specified height so initial time and distance offsets must be calculated. In the FG5, the mass begins to free fall for 20 ms to 30 ms before the data acquisition system is initialized to $t = 0$; this introduces a displacement of about 5 mm between the start of the drop and the start of data acquisition. We choose to reference the gravitational

acceleration to the top of the drop g_{top} ($z = 0$), rather than report g_0 for time $t = 0$. The relation between these two terms is

$$g_t = g_0 - \gamma z_0.$$

References

1. Kibble B. P., Robinson L. A., Bellis J. H., Redefining the Kilogram via a Moving Coil Apparatus, *CPEM 1990 Digest,* Ottawa, Canada, IEEE, 178-179.
2. Preston-Thomas H., Turnbull L., Green E., Dauphinee T., Kalra S., An Absolute Measurement of the Acceleration due to Gravity at Ottawa, *Can. J. Phys.,* 1960, **38**, 824-52.
3. Faller J. E., An Absolute Interferometric Determination of the Acceleration of Gravity, Ph.D. thesis, Princeton University, 1963.
4. Sakuma A., In *Recent Developments in Absolute Measurement Gravitational Acceleration,* Natl. Bur. Stand. (US) Spec. Pub. 343, 1970, 447-456.
5. Cook A., The Absolute Determination of the Acceleration due to Gravity, *Metrologia,* 1965, **1**, 84-114.
6. Marson I., Faller J. E., g – The Acceleration Of Gravity: Its Measurement And Importance, *J. Phys. E.,* 1986, **19**, 22-32.
7. Hammond J. E., A Laser-Interferometer System for the Absolute Determination of the Acceleration of Gravity, Ph.D. thesis, University of Colorado, Boulder, 1970.
8. Zumberge M. R., Rinker R., Faller J. E., A Portable Apparatus for Absolute Measurements of the Earth's Gravity, *Metrologia,* 1982, **18**, 145-152.
9. Niebauer T. M., Hoskins J. K., Faller J. E., Absolute Gravity: A Reconnaissance Tool For Studying Vertical Crustal Motions, *J. Geophys. Res.,* 1986, **91**, 9145-9149.
10. Peter G., Moose R., Wessells C., Faller J., Niebauer T., New High-Precision Absolute Gravity Observations in the United States, *J. Geophys. Res.,* 1989, **94**, 565-5674.
11. Niebauer T. M., Faller J. E., Continuous Gravity Observations using Joint Institute for Laboratory Astrophysics Absolute Gravimeters, *J. Geophys. Res.,* 1992, **97**, 12427-12435.
12. Niebauer T. M., Faller J. E., Absolute Gravimetry: Environmental Noise Limits, In Proc. Workshop on Non Tidal Gravity Changes: Intercomparison between Absolute and Superconducting Gravimeters, Walferdange (Luxembourg), *Cahiers du Centre Européen de Géodynamique et de Seismologie,* 1991, **3**, 39-44.
13. Carter W. E., Peter G., Sasagawa G. S., Klopping F. J., Berstis K. A., Hilt R. L., Nelson P., Christy G. L., Niebauer T. M., Hollander W., Seeger H., Richter B., Wilmes H., Lothhammer A., New Gravity Meter Improves Measurements, *EOS,* 1994, **75**, 90-92.
14. Rinker R., Super Spring – A New Type of Low-Frequency Vibration Isolator, Ph.D. thesis, University of Colorado, Boulder, 1983.
15. Nelson P. G., An Active Vibration Isolation System For Inertial Reference And Precision Measurement, *Rev. Sci. Instrum.,* 1991, **62**, 2069-2075.
16. Niebauer T. M., Faller J. E., Godwin H. M., Hall J. L., Barger R. L., Frequency Stability Measurements on Polarization-Stabilized He-Ne Lasers, *Appl. Opt.,* 1988, **27**, 1285-1289.
17. Liard J., Courtier N., Canada's Contribution to the 1989 International Comparison of Absolute Gravimeters at the BIPM, *Bull. Inf. Bur. Grav. Int.,* 1991, **68**, 45-61.
18. Chartier J.-M., Labot J., Sasagawa G., Niebauer T.,

Hollander W., A Portable Iodine Stabilized He-Ne Laser and its Use in an Absolute Gravimeter, *IEEE Trans. Instrum. Meas.*, 1993, **42**, 420-422.

19. *BIPM Proc.-Verb. Com. Int. Poids et Mesures*, 1992, **60**, 23 p., Recommendation 3, CI-1992.

20. Niebauer T. M., The Effective Measurement Height of Free-fall Absolute Gravimeters, *Metrologia*, 1989, **26**, 115-118.

21. Niebauer T. M., McHugh M. P., Faller J. E., Galilean Test for the Fifth Force, *Phys. Rev. Lett.*, 1987, **59**, 609-612.

22. Niebauer T., New Absolute Gravity Instruments For Physics And Geophysics, Ph.D. thesis, University of Colorado, Boulder, 1987.

23. Zumberge M., A Portable Apparatus for Absolute Measurements of the Earth's Gravity, Ph.D. thesis, University of Colorado, Boulder, 1981.

24. Kennard E. H., *Kinetic Theory Of Gases*, New York, McGraw-Hill, 1938, 60-63, 291-337.

25. Klopping F. J., Peter G., Robertson D. S., Berstis K. A., Moose R. E., Carter W. E., Improvements in Absolute Gravity Observations, *J. Geophys. Res.*, 1991, **96**, 8295-8303.

26. Monchalin J. P., Kelly M. J., Thomas J. E., Kurnit N. A., Szoeke A., Zernike F., Lee P. H., Javan A., Accurate Laser Wavelength Measurement with a Precision Two-Beam Scanning Michelson Interferometer, *Appl. Opt.*, 1981, **20**, 736-757.

27. Peck E. R., Theory Of Cornercube Interferometer, *J. Opt. Soc. Am.*, 1948, **38**, 1015-1024.

28. Niebauer T. M., Faller J. E., Quinn T. J., Giacomo P., Path length changes in corner cubes, unpublished, 1993.

29. Ball Corporation Efratom Division, *Precision Time and Frequency Handbook*, Irvine, California, Ball Corporation, 1991.

30. Melchior P., *The Tides of the Planet Earth*, Oxford, Pergamon Press, 1983.

31. Baker T., Tidal deformations of the Earth, *Sci. Prog. Oxf.*, 1984, **69**, 197-233.

32. Farrell W., Deformation of the Earth by surface loads, *Rev. Geophys. Space Physics*, 1972, **10**, 761-797.

33. Rabbel W., Zschau J., Static Deformations and Gravity Changes at the Earth's Surface due to Atmospheric Loading, *J. Geophys.*, 1985, **93**, 81-99.

34. Van Dam T., Wahr J., Displacements of the Earth's surface due to atmospheric loading: effects on gravity and baseline measurements, *J. Geophys. Res.*, 1987, **92**, 1281-1286.

35. Wahr J., Deformation induced by polar motion, *J. Geophys. Res.*, 1979, **84**, 165-170.

36. Aki K., Richards P., *Quantitative Seismology – Theory and Methods*, Vol. 1, New York, W. H. Freeman, 1980.

37. Sasagawa G., Klopping F., Niebauer T. M., Faller J. E., Hilt R. L., Intracomparison Tests of Precision of the FG5 Absolute Gravity Meters, *Geophys. Res. Lett.*, 1994, submitted.